

Crystallography on curved surfaces

Vincenzo Vitelli^{*†‡}, J. B. Lucks[†], and D. R. Nelson[†]

^{*}Department of Physics and Astronomy, University of Pennsylvania, Philadelphia, PA 19104-6396; and [†]Lyman Laboratory of Physics, Harvard University, Cambridge, MA 02138

Edited by Tom C. Lubensky, University of Pennsylvania, Philadelphia, PA, and approved May 30, 2006 (received for review April 5, 2006)

We study static and dynamical properties that distinguish 2D crystals constrained to lie on a curved substrate from their flat-space counterparts. A generic mechanism of dislocation unbinding in the presence of varying Gaussian curvature is presented in the context of a model surface amenable to full analytical treatment. We find that glide diffusion of isolated dislocations is suppressed by a binding potential of purely geometrical origin. Finally, the energetics and biased diffusion dynamics of point defects such as vacancies and interstitials are explained in terms of their geometric potential.

dislocations | elasticity | geometric frustration | topological defects

The physics of 2D crystals on curved substrates is emerging as an intriguing route to the engineering of self-assembled systems such as the “colloidosome,” a colloidal armor used for drug delivery (1), devices based on ordered arrays of block copolymers that are a promising tool for “soft lithography” (2, 3), and liquid–solid domains in vesicles (4, 5). Curved crystalline order also affects the mechanical properties of biological structures like clathrin-coated pits (6, 7) or HIV viral capsids (8, 9) whose irregular shapes appear to induce a nonuniform distribution of disclinations in their shell (10).

In this article, we present a theoretical and numerical study of point-like defects in a soft crystalline monolayer grown on a rigid substrate of varying Gaussian curvature. We suppose that the monolayer has a lattice constant of order, say, 10 nm or more. The substrate can then be assumed smooth, as would be the case for monolayers composed of di-block copolymers (2, 3). Disclinations and dislocations are important topological defects that induce long-range disruptions of orientational or translational order, respectively (ref. 11 and references therein and ref. 12). Disclinations are points of local 5- and 7-fold symmetry in a triangular lattice (labeled by topological charges $q = \pm\frac{2\pi}{6}$), whereas dislocations are disclination dipoles characterized by a Burger’s vector, \mathbf{b} , defined as the amount by which a circuit drawn around the dislocation fails to close (see Fig. 1 *Inset*). Other point defects such as vacancies, interstitials, or impurity atoms create shorter-range disturbances that introduce only local stretching or compression in the lattice (see Fig. 5). Such defects are important for particle diffusion and relaxation of concentration fluctuations.

These particle-like objects interact not only with each other, but also with the curvature of the substrate by a one-body geometric potential that depends on the particular type of defect (13, 14). These geometric potentials are in general nonlocal functions of the Gaussian curvature that we determine explicitly here for a model surface shaped as a “Gaussian bump.” An isolated bump of this kind models long wavelength undulations of a lithographic substrate, has regions of both positive and negative curvature, and yet is simple enough to allow straightforward analytic and numerical calculations. The presence of these geometric potentials triggers defect-unbinding instabilities in the ground state of the curved space crystal, even if no topological constraints on the net number of defects exist. Geometric potentials also control the dynamics of isolated dislocations by suppressing motion in the glide direction. Similar mechanisms influence the equilibrium distribution and dynamics of vacancies, interstitials, and impurity atoms.

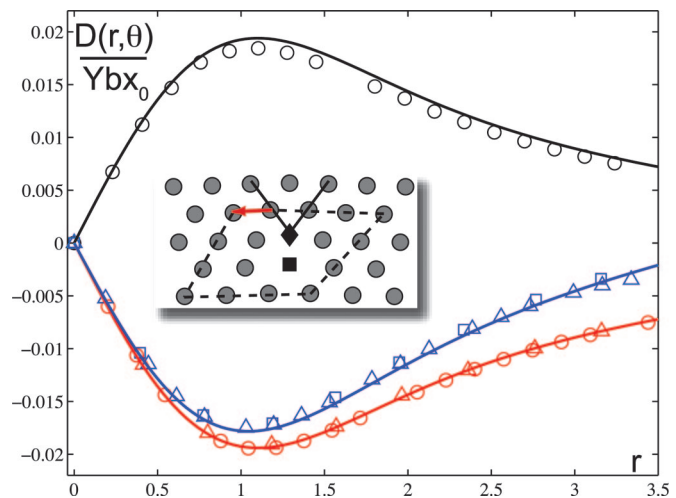


Fig. 1. The dislocation potential $D(r, \theta = \pm\frac{\pi}{2})$ in Eq. 17 (including boundary corrections) is plotted as a continuous line for a Gaussian bump parameterized by $\alpha = 0.5$ in the limit $R \gg x_0 \gg a$. Open symbols represent the numerical minimization of a fixed connectivity harmonic model for which the separation of the positive or negative disclination pair representing the dislocation is fixed while varying the dimensionless radial distance $|x|/x_0$ of the dislocation from the bump. An angle $\theta = \frac{\pi}{2}$ indicates that the positive disclination is closer to the top of the bump. Lower branch: $\theta = \pi/2$, $R/x_0 = 4$ (blue), 8 (red); and $x_0/a = 10$ (○), 20 (△), and 40 (□). Upper branch: $\theta = -\pi/2$, $R/x_0 = 8$, and $x_0/a = 10$. (*Inset*) A schematic view of a dislocation with filled symbols representing six-coordinate (circles), five-coordinate (diamond), and seven-coordinate (square) particles. Also depicted are the two rows of extra atoms emanating from the five-coordinated particle. The Burger’s vector is shown as a red arrow, completing the circuit around the dislocation (dashed line).

Basic Formalism

The in-plane elastic free energy of a crystal embedded in a gently curved frozen substrate, given in the Monge form by $\mathbf{r}(x, y) = (x, y, h(x, y))$, can be expressed in terms of the Lamé coefficients μ and λ (15):

$$F = \frac{1}{2} \int dA \sigma_{ij}(\mathbf{x}) u_{ij}(\mathbf{x}) = \int dA \left(\mu u_{ij}^2(\mathbf{x}) + \frac{\lambda}{2} u_{kk}^2(\mathbf{x}) \right), \quad [1]$$

where $\mathbf{x} = \{x, y\}$ represents a set of standard Cartesian coordinates in the plane and $dA = dx dy \sqrt{g}$, where $\sqrt{g} = \sqrt{1 + (\partial_x h)^2 + (\partial_y h)^2}$. In Eq. 1, the stress tensor $\sigma_{ij}(\mathbf{x}) = 2\mu u_{ij}(\mathbf{x}) + \lambda \delta_{ij} u_{kk}(\mathbf{x})$ was written in terms of the strain tensor $u_{ij}(\mathbf{x}) = \frac{1}{2} [\partial_i u_j(\mathbf{x}) + \partial_j u_i(\mathbf{x}) + A_{ij}(\mathbf{x})]$. The latter contains an additional term $A_{ij}(\mathbf{x}) = \partial_i h(\mathbf{x}) \partial_j h(\mathbf{x})$ (compared with its flat-space counterpart) that couples the gradient of the displace-

Conflict of interest statement: No conflicts declared.

This paper was submitted directly (Track II) to the PNAS office.

Freely available online through the PNAS open access option.

[†]To whom correspondence should be addressed. E-mail: vitelli@sas.upenn.edu.

© 2006 by The National Academy of Sciences of the USA

ment field $u_i(\mathbf{x})$ to the geometry of the substrate as embedded in the gradient of the substrate height function $h(\mathbf{x})$. We will often illustrate our results for a single Gaussian bump whose height function is given by:

$$h(\mathbf{x}) = \alpha x_0 e^{-\frac{r^2}{2}}, \quad [2]$$

where $r \equiv |\mathbf{x}|/x_0$ is the dimensionless radial coordinate (16). The aspect ratio α provides a dimensionless control parameter to measure deviations from flatness.

In Eq. 1 and the rest of this article, we adopt the ordinary flat-space metric (e.g., setting $dA \approx dx dy$) and absorb all of the complications associated with the curved substrate into the tensor field $A_{ij}(\mathbf{x})$ that resembles the more familiar vector potential of electromagnetism. Like its electromagnetic analog, the curl of the tensor field $A_{ij}(\mathbf{x})$ has a clear physical meaning and is equal to the Gaussian curvature of the surface $G(\mathbf{x}) = -\varepsilon_{ij}\varepsilon_{jk}\partial_l\partial_k A_{ij}(\mathbf{x})$, where ε_{ij} is the antisymmetric unit tensor ($\varepsilon_{xy} = -\varepsilon_{yx} = 1$) (14). The consistency of our perturbative formalism to leading order in α is demonstrated in Appendix 1, which is published as supporting information on the PNAS web site.

Minimization of the free energy in Eq. 1 with respect to the displacements $u_i(\mathbf{x})$ naturally leads to the force-balance equation, $\partial_i\sigma_{ij}(\mathbf{x}) = 0$. If we write $\sigma_{ij}(\mathbf{x})$ in terms of the Airy stress function $\chi(\mathbf{x})$:

$$\sigma_{ij}(\mathbf{x}) = \varepsilon_{il}\varepsilon_{jk}\partial_l\partial_k\chi(\mathbf{x}), \quad [3]$$

then the force balance equation is automatically satisfied,

$$\partial_i\sigma_{ij} = \varepsilon_{jk}\partial_k[\partial_1, \partial_2]\chi(\mathbf{x}) = 0, \quad [4]$$

because the commutator of partial derivatives is zero. However, we must be able to extract from $\chi(\mathbf{x})$ the correct $u_{ij}(\mathbf{x})$ that incorporates the geometric constraint of Eq. 2 and accounts for the presence of any defects. These requirements are enforced by solving a biharmonic equation for $\chi(\mathbf{x})$ whose source is controlled by the varying Gaussian curvature of the surface $G(\mathbf{x})$ and the defect density $S(\mathbf{x})$ (11, 14):

$$\frac{1}{Y}\Delta^2\chi(\mathbf{x}) = S(\mathbf{x}) - G(\mathbf{x}). \quad [5]$$

In the special case $S(\mathbf{x}) = 0$, we denote the solution of Eq. 5 as $\chi^G(\mathbf{x})$ where the superscript G indicates that the Airy function and the corresponding stress tensor $\sigma_{ij}^G(\mathbf{x})$ describe elastic deformations caused by the Gaussian curvature $G(\mathbf{x})$ only, without contribution from the defects. The stress of geometric frustration, $\sigma_{ij}^F(\mathbf{x})$, is a nonlocal function of the curvature of the substrate and plays a central role in our treatment of curved-space crystallography. The Young modulus $Y = \frac{4\mu(\mu + \lambda)}{2\mu + \lambda}$ (11, 12) naturally arises upon recasting (up to boundary terms) the free energy in Eq. 1 as a simple functional of the scalar field $\chi(\mathbf{x})$:

$$F = \frac{1}{2Y} \int dA (\Delta\chi(\mathbf{x}))^2. \quad [6]$$

The source $S(\mathbf{x})$ for a distribution of N unbound disclinations with “topological charges” $\{q_\alpha = \pm\frac{2\pi}{6}\}$ and M dislocations with Burger’s vectors $\{\mathbf{b}^\beta\}$ reads (11):

$$S(\mathbf{x}) = \sum_{\alpha=1}^N q_\alpha \delta(\mathbf{x}, \mathbf{x}^\alpha) + \sum_{\beta=1}^M \varepsilon_{ij} b_i^\beta \partial_j \delta(\mathbf{x}, \mathbf{x}^\beta), \quad [7]$$

where $|\mathbf{b}|$ is equal to the lattice constant a for dislocations with the smallest Burger’s vector. For N isotropic vacancies, interstitials, or impurities, we have (11):

$$S(\mathbf{x}) = \frac{1}{2} \sum_{\alpha=1}^N \Omega_\alpha \Delta \delta(\mathbf{x}, \mathbf{x}^\alpha), \quad [8]$$

where $\Omega_\alpha \sim a^2$ is the local area change caused by including the point defect at position \mathbf{x}^α .

To determine the geometric potential of a defect (on a deformed plane flat at infinity), we integrate by parts twice in Eq. 6 and use Eq. 5 to obtain $\Delta^2\chi(\mathbf{x})$ and $\chi(\mathbf{x})$ in terms of the Green’s function of the biharmonic operator:

$$F = \frac{Y}{2} \int dA \int dA' (S(\mathbf{x}) - G(\mathbf{x})) \frac{1}{\Delta_{xx'}} (S(\mathbf{x}') - G(\mathbf{x}')). \quad [9]$$

It is convenient to introduce an auxiliary function $V(\mathbf{x})$ that satisfies the Poisson equation $\Delta V(\mathbf{x}) = G(\mathbf{x})$ and vanishes at infinity where the surface flattens out. The geometric potential, $\zeta(\mathbf{x}^\alpha)$, of a defect at \mathbf{x}^α follows from integrating by parts the cross terms (involving the source and the Gaussian curvature) in Eq. 9 with the result:

$$\zeta(\mathbf{x}^\alpha) = -Y \int dA' S(\mathbf{x}') \int dA \frac{1}{\Delta_{xx'}} V(\mathbf{x}). \quad [10]$$

This formula ignores defect self-energies⁸ and needs to be supplemented by boundary corrections, as discussed in Appendix 2, which is published as supporting information on the PNAS web site.

In the following sections, we explicitly show that our results derived from Eq. 10 can also be obtained by means of more heuristic arguments. According to this point of view, defects introduced in the curved-space crystal are local probes of the preexisting stress of geometric frustration $\sigma_{ij}^G(\mathbf{x})$ to which they are coupled by intuitive physical mechanisms such as Peach-Koehler forces.

Geometric Frustration

We start by calculating the energy of a relaxed defect-free 2D crystal on a quenched topography. In analogy with the bending of thin plates we expect some stretching to arise as an unavoidable consequence of the geometric constraints associated with the Gaussian curvature (15). The resulting energy of geometric frustration, F_0 , can be estimated with the aid of Eq. 5, which, when $S(\mathbf{x}) = 0$, reduces to a Poisson equation whose source is given by $V(\mathbf{x})$:

$$\frac{1}{Y}\Delta\chi^G(\mathbf{x}) = -V(\mathbf{x}) + H_R(\mathbf{x}). \quad [11]$$

where $H_R(\mathbf{x})$ is an harmonic function of \mathbf{x} parameterized by the radius of the circular boundary R . $H_R(\mathbf{x})$ vanishes in the limit $R \gg x_0$ if free boundary conditions are chosen. Using the general definition of the Airy function (Eq. 3), we obtain:

$$\sigma_{kk}^G(\mathbf{x}) = \Delta\chi^G(\mathbf{x}) = -YV(\mathbf{x}). \quad [12]$$

⁸For dislocations, vacancies, and interstitials, the position-dependent self-energies can be ignored compared with $\zeta(\mathbf{x}^\alpha)$, because they are proportional to higher powers of the lattice spacing a .

For a surface with azimuthal symmetry, like the bump, the only nonvanishing components of the stress tensor of geometric frustration $\sigma_{ij}^G(\mathbf{x})$ read:

$$\sigma_{\phi\phi}^G(r) = \frac{1}{x_0^2} \frac{\partial^2 \chi^G}{\partial r^2}. \quad [13]$$

$$\sigma_{rr}^G(r) = \frac{1}{x_0^2 r} \frac{\partial \chi^G}{\partial r}. \quad [14]$$

and Poisson's equation can be readily solved upon applying Gauss' theorem with the Gaussian curvature $G(r) \approx \alpha^2 e^{-r^2} (1 - r^2)/x_0^2$ as a source (16):

$$V(r) = -x_0^2 \int_r^\infty \frac{dr'}{r'} \int_0^{r'} dr'' r'' G(r'') = -\frac{1}{4} \alpha^2 e^{-r^2}. \quad [15]$$

The extra factors of x_0 in the previous equations arise from expressing our results in terms of the dimensionless radial distance r .

Substituting Eq. 11 in Eq. 6, we have:

$$F_0 \approx \frac{Y}{2} \int dA V(r)^2 = \frac{Y\pi x_0^2 \alpha^4}{64}. \quad [16]$$

The result in Eq. 16 is valid to leading order in α , consistent with the assumptions of our formalism after taking the limit $R \gg x_0$. For a harmonic lattice, $Y = 2/\sqrt{3}k$, where k is an effective spring constant that can be extracted from more realistic interparticle potentials (17). For colloidal particles, k is typically two orders of magnitude larger than $k_B T/a^2$, where T is room temperature (18). Our numerical calculations of F_0 in fixed-connectivity harmonic solids are in good agreement with the small α expansion in Eq. 16 as long as the aspect ratio α is $\approx 1/2$ or lower (see Fig. 6, which is published as supporting information on the PNAS web site, for a numerical plot of F_0 versus α). An immediate implication of the geometric frustration embodied in Eqs. 15 and 16 is that nucleation of crystal domains on the bump will take place preferentially away from the top in regions where the surface flattens out.

Geometric Potential for Dislocations

The energy of a 2D curved crystal with defects will include the frustration energy, the interdefect interactions (to leading order these are unchanged from their flat-space form), possible core energies, and a characteristic, one-body potential of purely geometrical origin that describes the coupling of the defects to the curvature given by Eq. 10. The geometric potential of an isolated dislocation, $\zeta(\mathbf{x}) \equiv D(\mathbf{x}, \theta)$, is a function of its position and of the angle θ that the Burger vector \mathbf{b} forms with respect to the radial direction (in the tangent plane of the surface; see Fig. 1). Upon setting all $q_\alpha = 0$ in Eq. 7 and substituting into Eq. 10, we obtain, for an isolated dislocation, the resulting function $D(r = |\mathbf{x}|/x_0, \theta)$:

$$D(r, \theta) = -Yb_i \varepsilon_{ij} \partial_j \int dA' \frac{1}{\Delta_{\mathbf{x}\mathbf{x}'}} \left(V(\mathbf{x}') + \frac{\alpha^2 x_0^2}{4R^2} \right) \approx Ybx_0 \frac{\alpha^2}{8} \sin \theta \left[\left(\frac{e^{-r^2} - 1}{r} \right) + \left(\frac{x_0}{R} \right)^2 r \right]. \quad [17]$$

In view of the azimuthal symmetry of the surface, Gauss' theorem as expressed in Eq. 15, was used in deriving the second equality in Eq. 17, which is a function only of the dimensionless

radial coordinate r . The first term in Eq. 17 corresponds to the $R \rightarrow \infty$ geometric potential obtained from Eq. 10, while the second term is a finite size correction arising from a circular boundary of radius R (see Appendix 2 for a detailed derivation). Eq. 17 is valid to leading order in perturbation theory, consistent with the small α approximation adopted in this work.

In Fig. 1 we present a detailed comparison between the theoretical predictions for the geometric potential $D(r, \theta)/Ybx_0$ plotted versus $r = |\mathbf{x}|/x_0$ as continuous lines and numerical data from constrained minimization of a harmonic solid on a bump with $\alpha = 0.5$, under conditions such that $R \gg x_0 \gg a$. (See Appendix 3 and Figs. 7 and 8, which are published as supporting information on the PNAS web site, for a discussion of our numerical approach.) The lower and upper branches of the graph are obtained from Eq. 17 by setting $\theta = \pm \frac{\pi}{2}$ and letting R/x_0 equal 4 (Fig. 1, blue curve) or 8 (Fig. 1, red curve). Indeed, the (scaled) data from simulations with different choices of x_0/a (see Fig. 1 legend) collapse on the two master-curves according to their ratio of R/x_0 . Two different curves arise because the dislocation interacts with the curvature directly and via its image. The image-mediated interaction is given by the R -dependent term in Eq. 17. The $\sin \theta$ dependence of $D(r, \theta)$ on the direction of the Burgers vector is revealed by Fig. 1, because the upper branch of the graph corresponding to the unstable equilibrium $\theta = -\frac{\pi}{2}$ is approximately symmetric to the lower one corresponding to $\theta = \frac{\pi}{2}$.

The analogy between the geometrical potential of the dislocation and the more familiar interaction of an electric dipole in an external field can be elucidated by regarding the dislocation as a charge neutral pair of disclinations whose dipole moment $qd_i = \varepsilon_{ij} b_j$ is a lattice vector perpendicular to \mathbf{b} that connects the two points of 5- and 7-fold symmetry. The geometric potential, $U(r)$, of a disclination of topological charge q interacting with the Gaussian curvature satisfies the Poisson equation $\Delta U(r) = -qV(r)$ as can be seen by substituting the source in Eq. 7 with all $\mathbf{b}^\beta = 0$ into Eq. 10. For small r , positive (negative) disclinations are attracted (repelled) from the center of the bump by the integrated background source $V(r)$, which increases for $r \leq 1$ like $\alpha^2 r^2$ and is multiplied by the 2D electric field $\frac{1}{r}$, resulting in a geometric force that increases linearly in r . If the positive disclination within the dipole is closer to the top, the force it experiences will be opposite and slightly less than the one experienced by the negative disclination that is further away from the top. As a result a "tidal" force will push the dislocation (as a whole) downhill as shown by the lower branch of the plot of Fig. 1. For large r , however, the source $V(r)$ saturates and the attractive force exerted on the positive disclination wins and drags the dislocation toward the bump. The minimum of the geometric potential occurs at $|x_{\min}| \approx 1.1x_0$, close to the circle of zero Gaussian curvature $|\mathbf{x}| = x_0$, as a result of the competing interactions of the two disclinations comprising the dislocation. If the orientation of the disclination dipole is flipped, the geometric potential changes sign. Similarly, if the sign of the Gaussian curvature is reversed, the sign of the geometric interaction flips. As a result, a dislocation close to a saddle will have its Burger vector oriented so that the closest disclination to the saddle is 7-fold coordinated.

The physical origin of the dislocation potential can be understood heuristically by considering dislocation climb, or the motion of the dislocation in the radial direction (Fig. 2). According to standard elasticity theory, a dislocation in an external stress field $\sigma_{ij}(\mathbf{x})$ experiences a Peach-Koehler force, $\mathbf{f}(\mathbf{x})$, given by $f_k(\mathbf{x}) = \varepsilon_{kj} b_i \sigma_{ij}(\mathbf{x})$ (19, 20). Similarly, a dislocation introduced into the curved 2D crystal will experience a Peach-Koehler force as a result of the preexisting stress field of geometric frustration $\sigma_{ij}^G(\mathbf{x}^\alpha)$ whose nondiagonal components vanish. This interpretation is consistent with the geometric potential derived in Eq. 17, provided we use Eq. 11 to write $D(\mathbf{x}) = b_i \varepsilon_{ij} \partial_j \chi^G$. With \mathbf{b} along

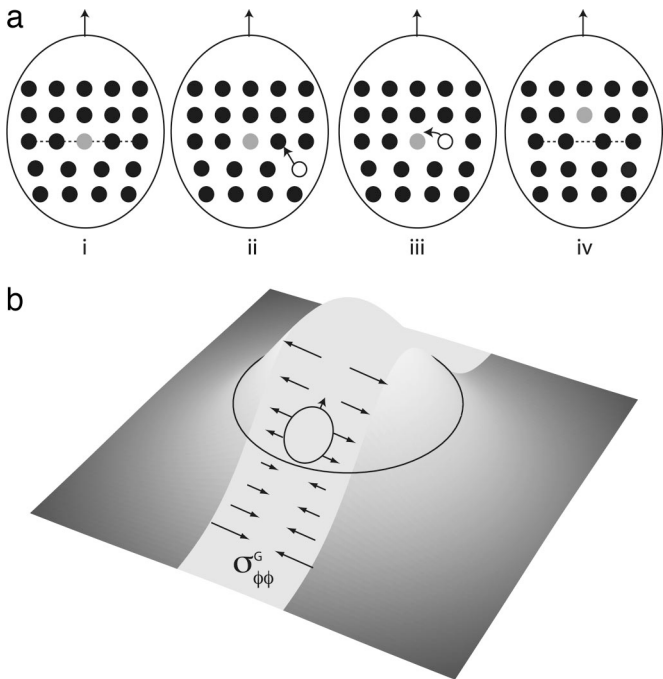


Fig. 2. Schematic of dislocation climb for the case of a square lattice. (a) Vacancy-mediated dislocation climb depicted in four steps: (i) Initial configuration consisting of an isolated dislocation (gray) (bonds in the third row are highlighted with dashed lines). (ii and iii) Motion of a vacancy (white) to the dislocation. (iv) Motion of the dislocation in the upward radial direction to create a configuration analogous to i. Comparison of the third row of atoms in i and iv reveals that this process results in overstretching of the bonds by a length of order of the lattice spacing a . (b) On a bump (outline of patch shown), the process represented in a is energetically unfavorable close to the top of the bump because there is a tensile stress $\sigma_{\phi\phi}^G$ (force per unit length indicated by arrows) that hinders further stretching of the bonds and tries to push the dislocation downward with a Peach–Koehler force $\sigma_{\phi\phi}^G b$, where the Burger’s vector $|b| \approx a$. The force changes sign at a distance of approximately x_0 from the top of the bump (black ring) where $\sigma_{\phi\phi}^G$ switches signs or if the direction of b is reversed.

its minimum orientation (azimuthal counterclockwise), we obtain a radial Peach–Koehler force of magnitude $f(r) = b\sigma_{\phi\phi}^G(r)$ that matches:

$$-\frac{1}{x_0} \frac{\partial D(r)}{\partial r} = \frac{b}{x_0^2} \frac{\partial^2 X^G(r)}{\partial r^2}$$

(see Eq. 13).

Dislocation Unbinding

If the 2D crystal is grown on a substrate that is sufficiently deformed, the resulting elastic strain can be partially relaxed by introducing unbound dislocations into the ground state (14, 16). Here, we present a simple estimate of the threshold aspect ratio, α_c , necessary to trigger this instability. Boundary effects will be ignored in what follows by letting $R \rightarrow \infty$ in Eq. 17.

Consider two dislocations located at \mathbf{x}_1 and \mathbf{x}_2 a distance of $\approx x_0$ from the center of the bump on opposite sides (see Fig. 3a Inset). Their disclination–dipole moments are opposite to each other and aligned in the radial direction so that the two (antiparallel) Burger’s vectors are perpendicular to the separation vector in the plane $\mathbf{x}_{12} \equiv \mathbf{x}_1 - \mathbf{x}_2$. In this case, the interaction between the dislocations reduces to $V_{12} \approx (Y/4\pi)b^2 \ln(|\mathbf{x}_{12}|/a)$ (11, 12). The instability occurs when the energy gain from placing each dislocation in the minima of the potential $D(\mathbf{x})$ given by Eq. 17 outweighs the sum of the work needed to tear them apart plus

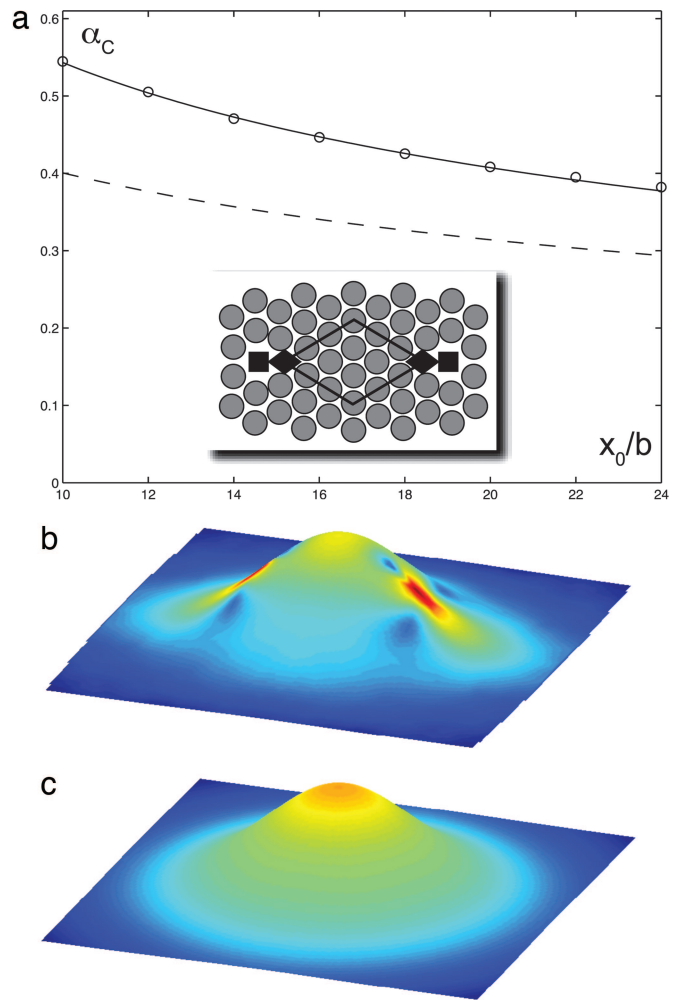


Fig. 3. Dislocation unbinding. (a) Critical aspect ratio, α_c , as a function of x_0/b . The theoretical estimate (18) is plotted vs. x_0/b for core energies $E_c = 0$ (dashed line) and the best fit $E_c = 0.1Yb^2$ (solid line). Numerical values (circles) were obtained as described in *Dislocation Unbinding* and Appendix 3. (Inset) Particle configuration projected in the plane for a dislocation pair straddling the bump. The extra atoms associated with the dislocations are highlighted with black lines. (b) Log of the numerical strain energy density on a bump for the configuration shown in Inset. (c) The same quantity for a defect-free bump. Both plots were constructed numerically with $x_0 = 10b$, $\alpha = 0.7 > \alpha_c$. Red represents high strain.

the core energies $2E_c$. The critical aspect ratio at the threshold that results is given by:

$$\alpha_c^2 \approx c \frac{b}{x_0} \ln\left(\frac{x_0}{b'}\right), \quad [18]$$

where $b' = (b/2)e^{-8\pi Ec/Yb^2}$ and $c \approx 1/2$. Note that the core energy E_c is determined by the microscopic physics of the particular system under study.

In Fig. 3a we present a comparison between Eq. 18 and numerical results. For each value of x_0/b , the corresponding α_c is obtained numerically by comparing the energy of a lattice without defects to the configuration with the two dislocations in their equilibrium positions. This interpretation for the origin of the instability is corroborated by the (numerical) strain energy density plots of Fig. 3b and c, where it is shown that introducing the pair of dislocations reduces the strain energy density on the top of the bump at the price of creating some large, but localized,

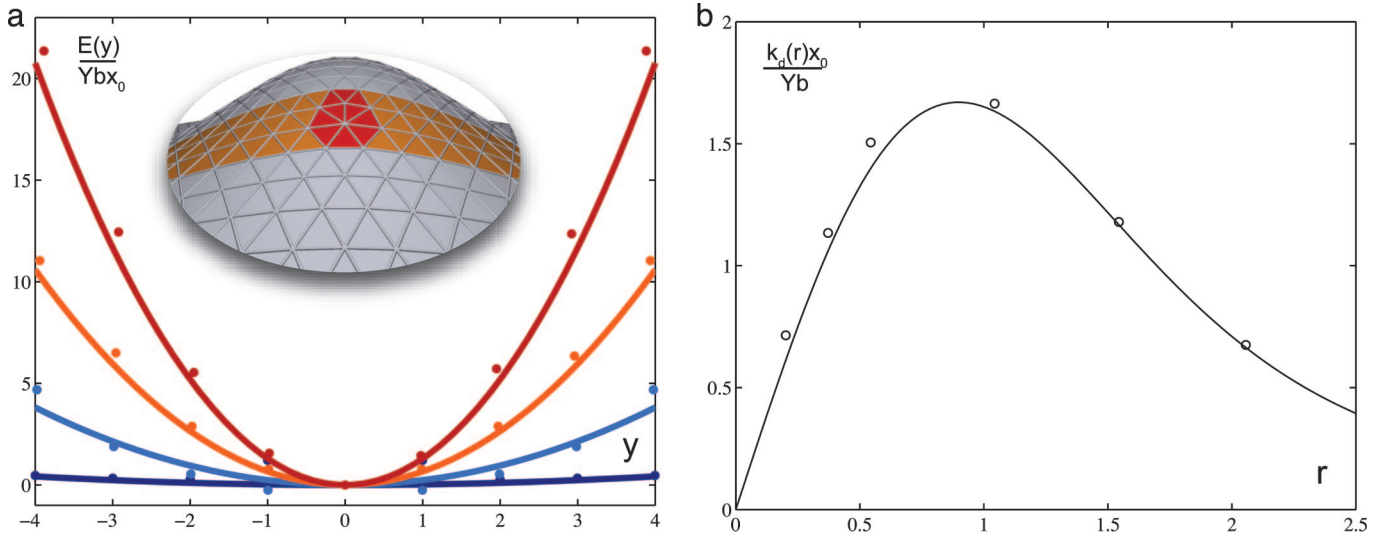


Fig. 4. Dislocation glide. (a) Filled circles represent numerical glide energies vs. distance along the glide direction y (units of a) for $x_0/a = 10$, $R/x_0 = 8$, $r = 0.5$ (at $y = 0$): $\alpha = 0.1$ (dark blue), 0.3 (blue), 0.5 (orange), and 0.7 (red). Solid lines represent $E(y) = \frac{1}{2}k_d y^2$, with k_d determined from Eq. 19. The energy is scaled by 10^{-4} . (Inset) Schematic of a dislocation (red) on a Gaussian bump. The glide path is highlighted in orange. (b) The curvature-induced glide-suppression spring constant $k_d(r)$ (19) (solid line) is plotted versus scaled in-plane distance from the top of the bump $r = |x|/x_0$ for $x_0 = 10a$, $\alpha = 0.5$. Open symbols represent numerical results found by fitting similar data as in a to parabolic curves in the glide coordinate. The ordinate axis is scaled by 10^{-2} .

strains around the dislocation cores where u_{ij} diverges. In the continuum limit $b \ll x_0$, very small deformations are enough to trigger the instability. This is the regime in which our perturbation treatment applies. As α is increased even further, a cascade of dislocation-unbinding transitions occurs involving larger numbers of dislocations and more complicated equilibrium arrangements of zero net Burger vector. For sufficiently large aspect ratios, we expect that the dislocations tend to line up in grain boundary scars similar to the ones observed in spherical crystals (1, 21). This scenario is consistent with preliminary results from Monte Carlo simulations in which the fixed-connectivity constraint is lifted and more complicated surface morphologies are considered (A. Hexamer, personal communication).

Glide Suppression

The dynamics of dislocations proceeds by means of two distinct processes: glide and climb. Glide describes motion along the direction defined by the Burger's vector; in flat space glide requires a very low activation energy and is the dominant form of motion at low temperature (see Fig. 4a Inset). Climb, or motion perpendicular to the Burger vector, requires diffusion of vacancies and interstitials (Fig. 2) and is usually frozen out relative to glide that involves only local rearrangements of atoms. On a curved surface, the geometric potential $D(r, \theta)$ imposes constraints on the glide dynamics of isolated dislocations, in sharp contrast to flat space where only small energy barriers are present because of the periodic Peierls potential (20).

As the dislocation represented in Fig. 4a Inset moves in the glide direction, it experiences a restoring potential generated by the variation of the (scaled) radial distance and the deviation from the radial alignment of the dislocation dipole. For a small transverse displacement, y , the harmonic potential $U(y) = \frac{1}{2}k_d y^2$ is controlled by a radial, position-dependent effective spring constant, k_d , which depends on the radial coordinate r . Upon expanding Eq. 17 to leading order in y and α , we obtain:

$$k_d(r) \approx \frac{\alpha^2 Y b}{4x_0} \left(\frac{1 - (1 + r^2)e^{-r^2}}{r^3} \right). \quad [19]$$

The harmonic potential $\frac{1}{2}k_d y^2$ is shown in Fig. 4a where the data obtained from numerical minimization of the harmonic lattice is

explicitly compared with the prediction of Eq. 19 for different values of the aspect ratio. Note that the effective spring constant plotted in Fig. 4b vanishes in the limit $b/x_0 \rightarrow 0$ but can still be important for small systems because Yb^2 can be of the order of hundreds of $k_B T \equiv \beta^{-1}$ (see *Geometric Frustration*). The confining potential plotted in Fig. 4a is similar to the one experienced by a dislocation bound to a disclination (18, 22).

The resulting thermal motion in the glide direction of dislocations in this binding harmonic potential can be modeled by an

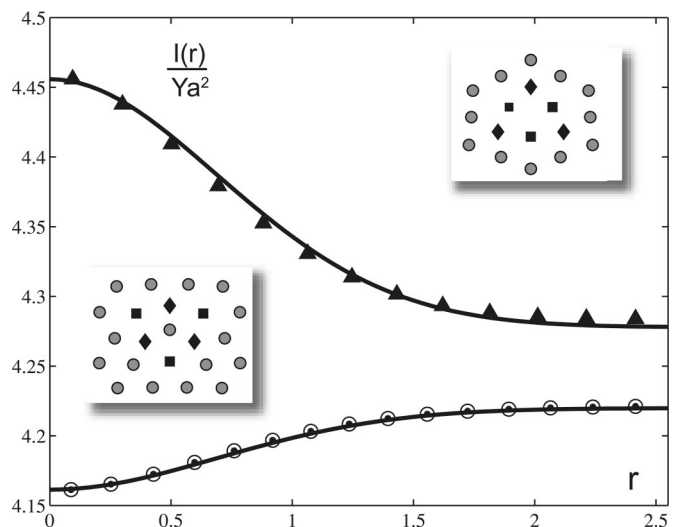


Fig. 5. The scaled potential energy $l(r)/Ya^2$ of interstitials (lower line) and vacancies (upper line) is plotted versus the scaled distance r for the same bump as Fig. 1. Solid lines were obtained from Eq. 20, where the area changes of interstitials and vacancies Ω_i^a and Ω_v^a were fit to the data. (Insets) Sample configurations are plotted. Diamonds, circles and squares represent 5-, 6-, and 7-fold coordinated particles, respectively. Filled and unfilled circles in the interstitial plot represent two distinct, but energetically equivalent, orientations of the disclination dipoles comprising the interstitial. They differ by swapping the 5- and 7-fold disclinations, which rotates the orientation of the filled, triangular plaquette by $\frac{\pi}{3}$.

overdamped Langevin equation for the glide coordinate y , leading to $\langle \Delta y^2 \rangle = (1 - e^{-2\mu K_d t})/\beta k_d$, where μ is the dislocation mobility (18, 22). In the case of a bump geometry, the effective spring constant k_d can be evaluated with Eq. 19. We emphasize, however, that the glide suppression mechanism considered here is not caused by the interaction of the dislocation with other defects but purely by the geometric interaction with the curvature of the substrate.

Vacancies, Interstitials, and Impurities

We now turn to a derivation of the geometric potential, $I(\mathbf{x})$, for interstitials, isotropic vacancies, and impurities. Inspection of Fig. 5 reveals that an interstitial (vacancy) can be viewed either as the product of locally adding (removing) an atom to the lattice or as a composite object made up of three disclination dipoles. To derive $I(\mathbf{x})$, we substitute the source term of Eq. 8 into Eq. 10 and integrate by parts twice. The result reads:

$$I(\mathbf{x}) \approx \frac{Y}{2} \Omega V(\mathbf{x}), \quad [20]$$

where boundary terms and a position-independent nucleation energy have been dropped. The constant Ω represents the area excess or deficit associated with the defect. In Fig. 5 a comparison of Eq. 20 with the results obtained from mapping out $I(r)$ numerically is presented. The area changes Ω_i and Ω_v for interstitials and vacancies, respectively, were fit to the numerical data. We find that Ω_v is negative and greater in magnitude than Ω_i . The large r behavior of $I(r)$ indicates that the core energy of a vacancy in flat space is greater than the one of an interstitial for the harmonic lattice. Interstitials tend to seek the top of the bump, whereas vacancies are pushed into the flat space regions. From the definition of $V(r)$ in Eq. 15, we deduce that an interstitial (vacancy) is attracted (repelled) by regions of positive (negative) Gaussian curvature similar to the behavior of an electrostatic charge interacting with a background charge distribution given by $-G(r)$. The function $V(r)$ controls the curvature-defect interaction for other types of defects such as disclinations in liquid crystals and vortices in ^4He films (16, 23). The expression for $V(r)$ in Eq. 15 reveals that $I(r)$ is indeed a nonlocal function of the Gaussian curvature determined as in electrostatics by the application of Gauss' law. Thus, the vacancy potential on a bump does not reach a minimum at the point where the Gaussian curvature is maximally negative but rather at infinity where the integrated Gaussian curvature vanishes.

We now argue heuristically how a localized point defect can couple nonlocally to the curvature and in the process we provide an alternative justification of Eq. 20 analogous to the informal

derivation of the dislocation potential. The energy cost of a defect at \mathbf{x}^α , $I(\mathbf{x}^\alpha)$, caused by local compression or stretching in the presence of an arbitrary elastic stress tensor $\sigma_{ij}(\mathbf{x})$ is given by $I(\mathbf{x}^\alpha) = p(\mathbf{x}^\alpha)\delta V$, where δV is the local volume change and $p(\mathbf{x}^\alpha)$ is the local pressure related to the stress tensor by $\sigma_{ij}(\mathbf{x}^\alpha) = -p(\mathbf{x}^\alpha)\delta_{ij}$ for the case of an isotropic stress (15). In two dimensions, we have $I(\mathbf{x}^\alpha) = -\sigma_{kk}(\mathbf{x}^\alpha)\Omega^\alpha/2$. We recover the result in Eq. 20, by assuming that the local deformation Ω^α (induced by the nucleation of a point defect) couples to the preexisting stress of geometric frustration $\sigma_{kk}^G = -YV(\mathbf{x})$ (see Eq. 12), which is a nonlocal function of the Gaussian curvature. Elastic deformations created by the geometric constraint throughout the curved 2D solid are propagated to the position of the point defect by force chains spanning the entire system. The point defect can then be viewed as a local probe of the stress field that does not measure the additional stresses induced by its own presence.

Note that the geometrical potential of an isotropic point defect is unchanged if we swap the 5- and 7-fold disclinations comprising it (corresponding to a rotation of the point defect by $\frac{\pi}{3}$ around its center), as demonstrated for interstitials in the lower branch of Fig. 5. Contrast this situation with the clear dipolar character of the dislocation potential plotted in Fig. 1. The more complicated case of nonisotropic point defects appears to still be captured qualitatively by Eq. 20; this was explicitly checked by plotting the geometric potential of "crushed vacancies" (24), which have both a lower symmetry and a lower energy than their isotropic counterparts.

An arbitrary configuration of weakly interacting point defects will relax to its equilibrium distribution by diffusive motion in a force field $\mathbf{f}(r) = -\nabla I(r)$. In overdamped situations, this geometric force leads to a biased diffusion dynamics with drift velocity

$$v \sim \beta |f| a \frac{D}{a} \sim \frac{\alpha^2 D Y \beta \Omega}{x_0},$$

where $\beta = 1/k_B T$ and D is the defect diffusivity (20). Eventually, a dilute gas of point defects equilibrates to a nonuniform spatial density proportional to $e^{-\beta I(r)}$.

We thank G. Chan, B. I. Halperin, A. Hexemer, Y. Kafri, R. D. Kamien, E. Kramer, A. Travesset, and A. M. Turner for stimulating conversations and the CrimsonGrid Initiative (Harvard University) for access to its computational resources. This work was supported by National Science Foundation Grant DMR-02-31631 and Harvard Materials Research Laboratory Grant DMR-02-13805. J.B.L. was supported by the Hertz Foundation. V.V. was supported by National Science Foundation Grants DMR-01-29804 and DMR-05-47230.

- Bausch, A. R., Bowick, M. J., Cacciuto, A., Dinsmore, A. D., Hsu, M. F., Nelson, D. R., Nikolaidis, M. G., Travesset, A. & Weitz, D. A. (2003) *Science* **299**, 1716–1718.
- Park, M., Harrison, C., Chaikin, P. M., Register, R. A. & Adamson D. H. (1997) *Science* **276**, 1401–1404.
- Kramer, E. J. (2005) *Nature* **437**, 824–825.
- Schneider, S. & Gompper, G. (2005) *Europhys. Lett.* **70**, 136–142.
- Chushak, S. & Travesset, A. (2005) *Europhys. Lett.* **72**, 767–773.
- Heuser, J. (1989) *J. Cell Biol.* **108**, 401–411.
- Kohyama, T., Kroll, D. M. & Gompper, G. (2003) *Phys. Rev. E* **68**, 061905.
- Ganser, B. K., Li, S., Klishko, V. Y., Finch, J. T. & Sundquist, W. I. (1999) *Science* **283**, 80–83.
- Li, S., Hill, C. P., Sundquist, W. I. & Finch, J. T. (2000) *Nature* **407**, 409–413.
- Toan, N., Bruinsma, R. F. & Gelbart, W. M. (2005) e-Print Archive, <http://arxiv.org/abs/physics/0506127>.
- Nelson, D. R. (2002) *Defects and Geometry in Condensed Matter Physics* (Cambridge Univ. Press, Cambridge, U.K.), pp. 217–238.
- Chaikin, P. M. & Lubensky, T. C. (1995) *Principles of Condensed Matter Physics* (Cambridge Univ. Press, Cambridge, U.K.).
- Bowick, M. J., Nelson, D. R. & Travesset, A. (2000) *Phys. Rev. B* **62**, 8738–8751.
- Sachdev, S. & Nelson, D. R. (1984) *J. Phys. C Solid State Phys* **17**, 5473–5489.
- Landau, L. D. & Lifshitz, E. M. (1999) *Theory of Elasticity* (Butterworth, Oxford).
- Vitelli, V. & Nelson, D. R. (2004) *Phys. Rev. E* **70**, 051105.
- Seung, S. & Nelson, D. R. (1988) *Phys. Rev. A* **38**, 1005–1018.
- Lipowsky, P., Bowick, M. J., Meinke, J. H., Nelson, D. R. & Bausch, A. R. (2005) *Nat. Mater.* **4**, 407–411.
- Weertman, J. & Weertman, J. R. (2002) *Elementary Dislocation Theory* (Oxford Univ. Press, New York), pp. 55–61.
- Kleman, M. & Lavrentovich, O. D. (2002) *Soft Matter Physics* (Springer, New York), pp. 261–299.
- Travesset, A. (2005) *Phys. Rev. E* **72**, 036110.
- Bruinsma, R., Halperin, B. I. & Zippelius, A. (1982) *Phys. Rev. B* **25**, 579–604.
- Vitelli, V. & Turner, A. M. (2004) *Phys. Rev. Lett.* **93**, 215–301.
- Jain, S. & Nelson, D. R. (2000) *Phys. Rev. E* **61**, 1599–1615.